Steady two-layer gravity-driven thin-film flow

Kamran Alba, Roger E. Khayat,* and Ramanjit S. Pandher
Department of Mechanical and Materials Engineering, The University of Western Ontario, London, Ontario, Canada N6A 5B9
(Received 2 April 2007; revised manuscript received 20 November 2007; published 8 May 2008)

Steady two-layer thin-film planar flow under gravity is investigated theoretically in this study. The film is assumed to emerge out of a channel and flow over a straight plate. The interplay among inertia, viscous and surface or interfacial tension is emphasized. It is found that the film and interface profiles, as well as the flow field, are strongly influenced by the viscosity ratio, film thickness ratio at inception, and surface-to-interfacial tension ratio. In the absence of surface and interfacial tension, the profiles of the film layers vary monotonically streamwise. The surface tension effect leads to waviness in layer profiles, with increasing wave number as the surface tension effect is reduced.

DOI: 10.1103/PhysRevE.77.056304 PACS number(s): 47.55.nd

I. INTRODUCTION

The steady flow of two superimposed Newtonian layers is examined theoretically in this study. The two-layer film is assumed to emerge from a channel and flow over a flat solid boundary. Although the flow of a single-layer film on a solid plate has been extensively investigated in the literature, little work has been devoted to multilayered films. One reason for the intense interest in thin-film flows is the wide variety of natural and industrial applications of such flows [1]. The influence of inertia, gravity, and substrate topography on steady flow and early stages of flow development of a single-layer Newtonian thin film, as it moves on a solid stationary substrate, was previously examined by Khayat and coworkers [2,3]. The pioneering work of Watson [4] focused on the steady laminar and turbulent radial and planar spread of a liquid jet over a horizontal plane, including the special case of two-dimensional flow. For a large distance from the source, a similarity solution of the laminar thin-film equations is sought. In particular, it is found that, for two-dimensional flow, the steady (dimensionless) shape of the free surface is given by $h^s = 1.81x/\mathrm{Re}$, where x is the distance from the source, and Re is the modified Reynolds number. This result was used by Khayat and Welke [2] to assess the validity of their formulation. The steady surface profile was obtained in the absence of gravity and surface tension. It constitutes an important limiting form. In the literature, most of the theoretical work has concentrated on Newtonian fluids [1,5], and to a much lesser extent on non-Newtonian fluids [6,7]. The effect of other external (body) forces, such as an electrostatic field, has also been examined on the flow of a film, its stability, and eventual rupture by Gorla and Byrd [8]. While most work in the literature has concentrated on the steady flow of the film over a straight substrate, some studies have focused on the effect of substrate topography. The steady free surface shape of thin-film flows over trenches and mounds was examined by Kalliadasis *et al.* [9]. Their study was limited, however, to surface-tension-dominated inertialess flows. They found that the free surface develops a ridge right before the entrance to the trench or exit from the mound, and that the ridge can become large for steep substrate features of significant depth. Earlier, Stillwagon and Larson [10] investigated this problem experimentally. They measured the changes in thickness of silicon oil films at the centers of holes and trenches of a silicon substrate using a noncontact interferometric technique. In this case, the flow was also surface tension dominated, and the inertia effect was negligible. Later, Stillwagon and Larson [11] considered the leveling of thin films over uneven substrates during spin coating.

Although the thin-film formulation reduces the pressure to its hydrostatic part, thus eliminating the momentum equation in the transverse direction from the problem, the dimension of the problem remains the same as in the original equation. At moderately high Reynolds number, inertia is better accounted for through the boundary-layer (BL) approximation, which includes the effect of transverse flow. The major difference between the original Navier-Stokes equations and the BL equations is the hydrostatic variation of pressure across the film depth. As a result, only the transverse momentum equation is eliminated, but the convective terms are retained in the remaining equations, and the number of boundary conditions is reduced. However, the solution of BL equations remains essentially as difficult to obtain as that of Navier-Stokes equations [12]. As proposed by Shkadov [13], a depthwise integration of the momentum equations in the transverse direction is usually performed by assuming a self-similar semiparabolic flow profile in the transverse direction. Although the depth-averaged BL equations are only of second order in time, they yield plausible results. The parabolic flow approximation is widely used in the literature, and its validity was established experimentally by Alekseenko *et al.* [14]. Recently, Ruschak and Weinstein [15] examined the gravity-driven flow of a thin film over a round-crested weir. The surface tension effect was neglected, while the inertia effect was included. The equations were depth averaged in the radial direction. Steady-state profiles of the free surface were obtained as functions of Reynolds number and weir diameter. More recently, Costa *et al.* [16] studied lava flow based on depth-averaged equations.

Multilayer film flow remains relatively unexplored, and has been considered mainly in relation to various applications in polymer processing, such as coextrusion and coinjection molding [17]. Thickness profiles and pressure drops

*rkhayat@uwo.ca

across ducts and channels in two- and three-layer flows have been measured and estimated in early studies [18–21]. These studies were motivated either to reduce the pressure drop or to study the interface deformation in the form of encapsulation of the viscous fluid by the fluid of low viscosity. The viscosity ratio is found to be the important parameter responsible as it affects the thickness and pressure drop. More recently, Anturkar *et al.* [22] studied multilayer Newtonian thin-film flow with application to extrusion and coating using depth-averaged equations. Although they included the surface tension effect, the inertia effect was neglected. Joseph *et al.* [23] carried out a linear stability analysis for the flow of two immiscible fluids of different viscosities and equal density in a pipe. They showed that the volume ratio, related to the fluid thicknesses, is a crucial factor for the interface shape and stability. Thereafter the instability of two cocurrent-superposed viscous fluids in a channel was examined by Hooper and Grimshaw [24]. They found that the interface may or may not be stable. In the latter case, the interface evolves to another steady state. Loewenherz and Lawrence [25] tackled the linear stability problem analytically for two-layer flow of fluids of equal density, in the absence of free surface and interfacial tension, and in the limit of Stokes flow. More recently, the interfacial stability for a two-layer film flowing under gravity through an inclined or vertical channel, as well as the free-surface two-layer flow down an inclined or vertical plane wall, were studied by Pozrikidis [26]. The analysis was carried out in the limit of Stokes flow.

The current study focuses on the influence of flow parameters, such as the viscosity ratio, velocity, and film thickness ratio at inception and the surface-to-interfacial tension ratio on two superimposed Newtonian thin films flowing on a solid and stationary substrate at a large distance from the source. The flow is analyzed first in the absence of surface and interfacial tension but fluid inertia is taken into account. Then the interplay between inertia and free surface and interfacial tension effects is investigated. The depth averaging approach is used by assuming a self-similar semiparabolic velocity profile for the streamwise velocity component. The paper is organized as follows. The problem formulation and solution procedure are given in Sec. II. The results and their discussion are presented in Sec. III, where steady flow behavior is covered. Finally, concluding remarks are given in Sec. IV.

II. PROBLEM FORMULATION AND SOLUTION PROCEDURE

In this section, the film flow configuration is introduced, and the scaled conservation equations for two-layer incompressible Newtonian film flow, as well as boundary conditions, are briefly discussed. The solution procedure is also outlined.

A. Thin-film equations and boundary conditions

Consider the two-layer gravity-driven flow of incompressible Newtonian fluids moving on a flat plate, making an angle θ with the horizontal. The two-layer film is assumed to emerge out of a channel and flow over the plate. Figure 1 displays schematically the flow configuration in the (X,Y) plane. Layers 1 and 2 are taken to correspond to the upper and lower layer, respectively, with $H_1(X)$ being the height of the free surface and $H_2(X)$ that of the interface. In this work, the two layers are assumed to have the same density ρ and different viscosities μ_1 and μ_2. Let σ_1 and σ_2 be the free-surface and interfacial tension coefficients, respectively. At inception $(X=0)$, layers 1 and 2 have heights H_{01} and H_{02}, and mean flow velocities U_{01} and U_{02}, respectively. Reference scales are conveniently introduced in terms of the geometric and flow parameters of the lower layer. In this case, H_{02} is taken as the length scale in the depthwise direction, and U_{02} is taken as the velocity scale streamwise. Consequently, the length scale in the streamwise direction is denoted by L, which is typically much larger than the film thickness $(L \gg H_{02})$. Assuming each layer to be thin, the following similarity parameters emerge in the problem, namely, the Reynolds number Re, Froude number Fr, capillary number Ca, thickness-to-length ratio ε, the height ratio R_H, viscosity ratio R_μ, and surface-tension ratio R_σ. More explicitly,

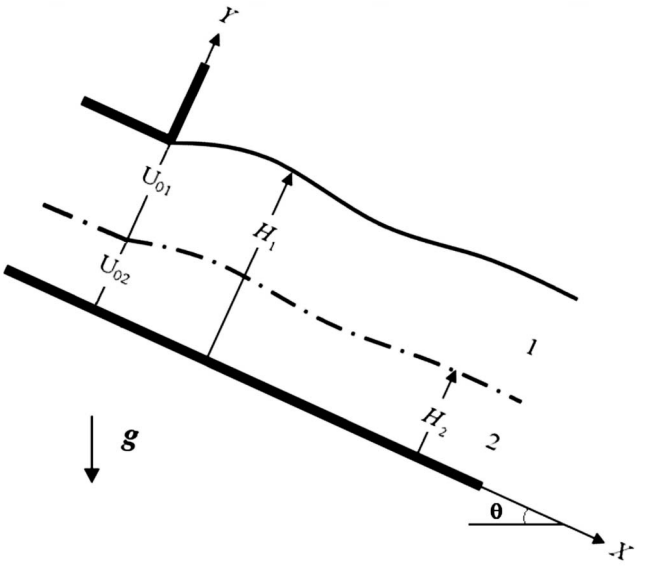

FIG. 1. Schematic illustration of two-layer thin-film flow exiting a channel. Dimensional notations are used.

$$\mathrm{Re} = \frac{\rho U_{02} H_{02}}{\mu_2}, \quad \mathrm{Fr} = \frac{U_{02}^2}{Lg}, \quad \mathrm{Ca} = \frac{\mu_2 U_{02}}{\sigma_2}, \quad \varepsilon = \frac{H_{02}}{L},$$

$$R_H = \frac{H_{01}}{H_{02}}, \quad R_\mu = \frac{\mu_1}{\mu_2}, \quad R_\sigma = \frac{\sigma_1}{\sigma_2}. \tag{1}$$

where g is the gravitational acceleration. The velocity scale is taken to correspond to Poiseuille flow in the channel, which, in this case, is given by

$$U_{02} = \frac{H_{02}^2 g \sin\theta}{2\nu_2}\left(\frac{(R_\mu - 1 + R_H^2)}{2(R_H + R_\mu - 1)} - \frac{1}{3}\right),$$

where $\nu_2 = \mu_2/\rho$ is the kinematic viscosity of the lower layer. Consequently, the Froude number can be expressed in terms of the remaining variables as

$$\mathrm{Fr} = \frac{\varepsilon}{2}\sin\theta\left(\frac{(R_\mu - 1 + R_H^2)}{2(R_H + R_\mu - 1)} - \frac{1}{3}\right)\mathrm{Re}.$$

This is an interesting relation as it shows the intricate interplay among gravity, inertia, viscosity ratio, and thickness ratio. The conservation equations for thin-film flow are obtained in dimensionless form, with terms of $O(\varepsilon^2)$ and higher being excluded. In this case, the relevant equations for the problem are

$$\frac{\partial u_1}{\partial x} + \frac{\partial v_1}{\partial y} = 0,$$

$$u_1\frac{\partial u_1}{\partial x} + v_1\frac{\partial u_1}{\partial y} = -\frac{1}{\mathrm{Re}\,\varepsilon}\frac{\partial p_1}{\partial x} + \frac{\sin\theta}{\mathrm{Fr}} + \frac{1}{\mathrm{Re}\,\varepsilon}R_\mu\frac{\partial^2 u_1}{\partial y^2},$$

$$\frac{\partial p_1}{\partial y} = -\mathrm{Re}\,\varepsilon^2\frac{\cos\theta}{\mathrm{Fr}} \tag{2}$$

for layer 1, and

$$\frac{\partial u_2}{\partial x} + \frac{\partial v_2}{\partial y} = 0,$$

$$u_2\frac{\partial u_2}{\partial x} + v_2\frac{\partial u_2}{\partial y} = -\frac{1}{\mathrm{Re}\,\varepsilon}\frac{\partial p_2}{\partial x} + \frac{\sin\theta}{\mathrm{Fr}} + \frac{1}{\mathrm{Re}\,\varepsilon}\frac{\partial^2 u_2}{\partial y^2},$$

$$\frac{\partial p_2}{\partial y} = -\mathrm{Re}\,\varepsilon^2\frac{\cos\theta}{\mathrm{Fr}} \tag{3}$$

for layer 2. Here u, v, and p are the dimensionless velocity components in the x and y directions, and the pressure, respectively, with subscripts corresponding to each layer. Note that εU_{02} and $\mu_2/\varepsilon^2 U_{02}L$ are taken as the velocity scale depthwise and the pressure scale, respectively. The dynamic conditions at the free surface reduce to (see Appendix A)

$$p_1 = -\left(\frac{R_\sigma\varepsilon^3}{\mathrm{Ca}}\right)h_1'', \quad \frac{\partial u_1}{\partial y} = 0 \quad \text{at } y = h_1. \tag{4}$$

At the interface,

$$p_2 - p_1 = -\left(\frac{\varepsilon^3}{\mathrm{Ca}}\right)h_2'', \quad R_\mu\frac{\partial u_1}{\partial y} = \frac{\partial u_2}{\partial y} \quad \text{at } y = h_2, \tag{5}$$

where $h_1(x)$ and $h_2(x)$ represent the dimensionless heights of free surface and interface, respectively. Here a prime denotes total differentiation. The kinematic conditions at the free surface and interface are given by

$$v_i(x, y = h_i) = h_i' u_i(x, y = h_i) \quad (i = 1,2) \tag{6}$$

No-slip and no-penetration conditions at the substrate are assumed, so that

$$u_2(x, y = 0) = v_2(x, y = 0) = 0. \tag{7}$$

The continuity of flow across the interface leads to

$$u_1(x, y = h_2) = u_2(x, y = h_2) \tag{8}$$

In this case, and assuming no mass transfer across the interface, the kinematic condition at the interface reads

$$v_1(x, y = h_2) = v_2(x, y = h_2). \tag{9}$$

At inception (x=0), the height of the free surface as well as that of the interface are assumed fixed, so that

$$h_1(x = 0) = R_\mathrm{H}, \quad h_2(x = 0) = 1. \tag{10}$$

In addition, the flow rate is also specified in each layer, or

$$\int_1^{R_H} u_1(x = 0, y)dy = \frac{R_H^4 + (-4 + 4R_\mu)R_H^3 + (-9R_\mu + 6)R_H^2 + (6R_\mu - 4)R_H + (-R_\mu + 1)}{R_\mu(R_H - 1)(3R_H^2 - 2R_H + R_\mu - 1)},$$

$$\int_0^1 u_2(x = 0, y)dy = 1. \tag{11}$$

B. Solution procedure

Upon using the dynamic conditions (4) and (5), the y-momentum equations in (2) and (3) yield the following expressions for the pressure in each layer, namely (see Appendix A),

$$p_1 = \mathrm{Re}\,\varepsilon^2\frac{\cos\theta}{\mathrm{Fr}}(h_1 - y) - \frac{R_\sigma\varepsilon^3}{\mathrm{Ca}}h_1'',$$

$$p_2 = \mathrm{Re}\,\varepsilon^2\frac{\cos\theta}{\mathrm{Fr}}(h_1 - y) - \frac{\varepsilon^3}{\mathrm{Ca}}(h_2'' + R_\sigma h_1''). \tag{12}$$

Substituting for pressure into the x-momentum equations finally gives

$$u_1\frac{\partial u_1}{\partial x} + v_1\frac{\partial u_1}{\partial y} = -\varepsilon\frac{\cos\theta}{\mathrm{Fr}}h_1' + \frac{1}{\mathrm{Re}}\frac{R_\sigma\varepsilon^2}{\mathrm{Ca}}h_1''' + \frac{\sin\theta}{\mathrm{Fr}} + \frac{1}{\mathrm{Re}\,\varepsilon}R_\mu\frac{\partial^2 u_1}{\partial y^2},$$

$$u_2\frac{\partial u_2}{\partial x} + v_2\frac{\partial u_2}{\partial y} = -\varepsilon\frac{\cos\theta}{\mathrm{Fr}}h_1' + \frac{1}{\mathrm{Re}}\frac{\varepsilon^2}{\mathrm{Ca}}(h_2''' + R_\sigma h_1''') + \frac{\sin\theta}{\mathrm{Fr}} + \frac{1}{\mathrm{Re}\,\varepsilon}\frac{\partial^2 u_2}{\partial y^2}, \tag{13}$$

which must be solved subject to conditions (6)–(11). In this study, a depth-averaging approach is implemented for the solution of the problem. Following the standard procedure for one-layer film flow [13–15], the profiles for the streamwise velocity component is assumed to be semiparabolic in y in each layer. Using conditions (6), the depthwise velocity component is then obtained upon integrating the continuity equation in each layer. Thus, upon letting $u_i(x,y)=A_i(x)y^2+B_i(x)y+C_i(x)$, it is not difficult to show that the coefficients can be expressed in terms of the mean velocity components $\bar{u}_1(x)$ and $\bar{u}_2(x)$, and heights $h_1(x)$ and $h_2(x)$, and the viscosity ratio, namely,

$$A_1 = \frac{(h_1-h_2)\left(\bar{u}_1 - \frac{3}{2}\bar{u}_2\right)}{f(h_1,h_2,R_\mu)},$$

$$A_2 = \frac{3}{2h_2^2}(R_\mu A_1 h_2^2 - R_\mu A_1 h_1 h_2 - \bar{u}_2),$$

$$B_1(x) = -2A_1h_1, \quad B_2(x) = 2R_\mu A_1 h_2 - 2R_\mu A_1 h_1 - 2A_2 h_2,$$

$$C_1(x) = 2A_1h_1h_2 - 2R_\mu A_1 h_1 h_2 - h_2^2 A_1 - h_2^2 A_2 + 2R_\mu A_1 h_2^2,$$

$$C_2(x) = 0, \tag{14}$$

where

$$f(h_1,h_2,R_\mu) = h_1h_2^2 - \frac{2h_1^3+h_2^3}{3} + \left(2h_1h_2 - h_2^2 - \frac{1}{2}R_\mu h_1 h_2 + \frac{1}{2}R_\mu h_2^2\right)(h_1-h_2).$$

Equations (13), along with the continuity equations in (3) and (4), can now be integrated over each layer to yield the following equations for the coefficients A_i and heights h_i $(i=1,2)$:

$$P_1A_1' + Q_1A_2' + R_1h_1' + S_1h_2' = 0,$$

$$P_2A_1' + Q_2A_2' + R_2h_1' + S_2h_2' = 0,$$

$$P_3A_1' + Q_3A_2' + R_3h_1' + S_3h_2' = \frac{2A_2h_2}{\mathrm{Re}\,\varepsilon} + \frac{\sin\theta}{\mathrm{Fr}}h_2 + \frac{\varepsilon^2}{\mathrm{Re\,Ca}}h_2(h_2''' + R_\sigma h_1'''),$$

$$P_4A_1' + Q_4A_2' + R_4h_1' + S_4h_2' = \frac{2R_\mu}{\mathrm{Re}\,\varepsilon}A_1(h_1-h_2) + \frac{\sin\theta}{\mathrm{Fr}}(h_1-h_2) + \frac{R_\sigma\varepsilon^2}{\mathrm{Re\,Ca}}(h_1-h_2)h_1''', \tag{15}$$

where the coefficients $P_\alpha, Q_\alpha, R_\alpha, S_\alpha$ $(\alpha=1,2,3,4)$ are explicit functions of A_1, A_2, h_1, h_2, and are given in Appendix B. Equations (15) are solved as an initial-value problem using a fourth-order Runge-Kutta integration scheme. The accuracy of the numerical scheme has been ensured by monitoring the constancy of the flow rate at different locations along the film flow.

III. RESULTS AND DISCUSSION

The formulation and numerical implementation above are now applied to investigate steady two-layer film flow. The effect of geometric and flow parameters on the film profile and flow field is investigated. The limiting case of one-layer flow is also discussed for reference. The effect of surface and interfacial tensions will be examined through the capillary number Ca and surface-to-interfacial tension ratio R_σ. Depending upon the level of the surface-tension effect, a regular and singular perturbation solution near inception is also obtained for one-layer film flow. Given the many parameters in the problem, the flow will be considered first in the absence of surface and interfacial tension effects. In this case, Ca $\sim O(\varepsilon)$ or larger. The influence of surface tension tends to be weak, for instance, for flow with dominant inertia. This has been particularly demonstrated for single-layer film. Lee and Mei [27] found that the surface-tension effect decreases strongly with increasing inertia. When cast in terms of the present similarity parameters, they showed that the capillary number behaves roughly as $\mathrm{Ca}\sim 1/\varepsilon$. The capillary number can in fact be large even for some flows with high viscosity, such as the flow of polybutene oils. As an illustration, consider polybutene fluid with average viscosity $\mu=80$ mPa s, density $\rho=1200$ kg m^{-3}, and surface-tension coefficient $\sigma=50$ mNm^{-1} flowing at average velocity of 12 ms^{-1}. For a film of 2 mm thickness at inception, $\varepsilon=1/360$ and Ca $=19.2$, making surface-tension effects clearly negligible in this case. This value of Ca is within the same order of magnitude as that encountered in polymer processing, such as the injection molding of polybutene [28]. Nevertheless, surface and interfacial tension effects will also be examined in detail.

A. Flow with negligible surface and interfacial tension

The typical flow field and layer shapes are depicted in Fig. 2. Although this flow case is relatively simple, it will serve as reference for the more complex flows below. The distributions of the velocity components along the free surface $h_1(x)$ and interface $h_2(x)$ are also shown. Both h_1 and h_2 tend to decrease overall with increasing x as a result of film contraction [Fig. 2(a)]. However, the interface exhibits a nonmonotonic decrease with a weak maximum near the channel exit. Generally, h_1 and h_2 decrease at the same rate. The emergence of a maximum at the interface is the result of a relatively strong vertical flow in the lower layer caused by the vicinity of the lower layer to the plate. This is further confirmed from Fig. 2(b), where the relative drop in the depthwise flow intensity between the interface and the free surface is generally more significant than the drop in the streamwise velocity. This drop is particularly large near inception as a result of strong elongation or the sharp increase in the streamwise velocity due to film contraction.

One of the most important dimensionless parameters appearing in two-layer flow problems is the viscosity ratio. This parameter is also a key factor in the onset of flow instability [29]. The overall dependence of the free surface and interfacial heights on viscosity ratio is illustrated in Fig. 3. Since the parametric flow response is expected to vary with position, both the heights close to the origin [at $x=1$ in Fig.

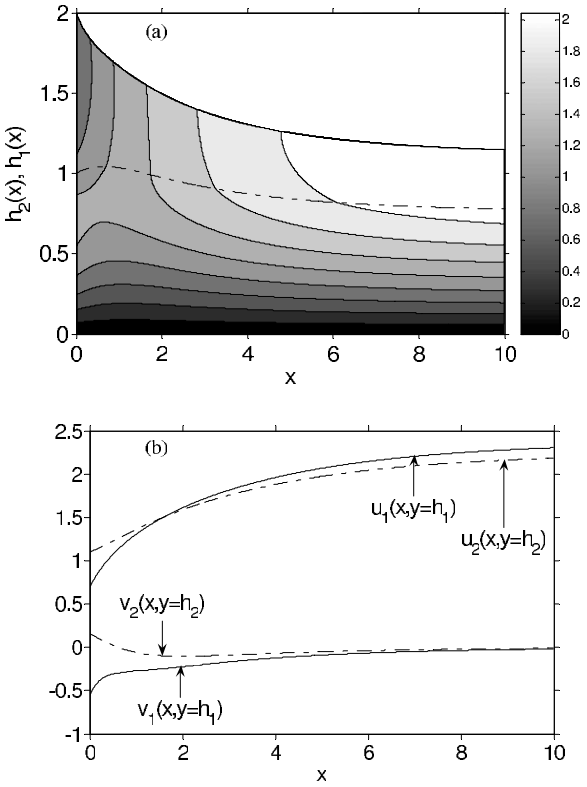

FIG. 2. Typical two-layer film flow for $\theta=90°$, $\varepsilon=0.1$, $R_\mu=2$, $R_H=2$, and Re=100. (a) shows the free surface (solid curve) and interface (dash-dotted curve) heights as well as the velocity magnitude contours. (b) displays the dependence of velocity components at the interface (dash-dotted lines) and free surface (solid lines) on x.

3(a)] and far downstream [at $x=10$ in Fig. 3(b)] are plotted against R_μ. Simultaneously, Fig. 4 displays the profiles of the free surface and interface at four different viscosity ratios. Figure 3(a) shows that the interface height remains relatively unaffected by the viscosity ratio near the origin, whereas the free surface height decreases essentially linearly. Further downstream, Fig. 3(b) shows that h_1 decreases less strongly with increasing R_μ, exhibiting two distinct slopes. This change in slope at some critical viscosity ratio is reminiscent of phase transition phenomena [30]. Although the interface displays a minimum in height, it remains relatively unaffected by the viscosity ratio. This is indeed confirmed from Fig. 4. For small R_μ, the relatively low viscosity of the upper layer prohibits its contraction as Fig. 4(a) indicates, with the layer behaving close to an inviscid fluid. As R_μ increases, a relatively sharp drop in height occurs in h_1, reflecting stronger contraction. The increase in viscosity ratio is equivalent to the thinning of the lower layer relative to the upper layer, which in turn leads to a less effective overall momentum transfer with the (stationary) plate. The increase in contraction is evident from Figs. 4(b)–4(d). For very high viscosity ratio ($R_\mu>10$), the two-layer film behaves like a one-layer film as a result of the strong gravitational effect relative to viscous effects.

Gravity plays an important role as a driving force. Indeed, in the absence of capillarity, the free surface and interface shapes depend only on the interplay between viscous forces and gravity. The effect of gravity can be examined by changing the plate angle (see also Fig. 11 in the presence of surface tension). Figure 5 depicts the influence of θ. The figure clearly illustrates the nonmonotonic response of film shape as gravity increases. For very small inclination angle ($\theta=1°$), the film is essentially flat, reflecting a film at rest. As θ increases while remaining small, viscous forces remain dominant, and the film grows with distance. Given the presence of gravity, the film does not grow linearly as in Watson's similarity solution [4]. For dominant gravity ($\theta>5°$), the film contracts, and reaches an asymptotic level far downstream [see Figs. 5(c) and 5(d)]. The behavior in Fig. 5 is similar to that encountered for one-layer flow. In the latter case, the film height $h(x)$ is dictated by the following equation (see Appendix C):

$$\left(\varepsilon\frac{\cos\theta}{\mathrm{Fr}}-\frac{6}{5h^3}\right)h'=-\frac{3}{\mathrm{Re}\,\varepsilon h^3}+\frac{\sin\theta}{\mathrm{Fr}}. \tag{16}$$

Note in this case that $\mathrm{Fr}=\varepsilon\mathrm{Re}\sin\theta/12$ so that Eq. (16) reduces to

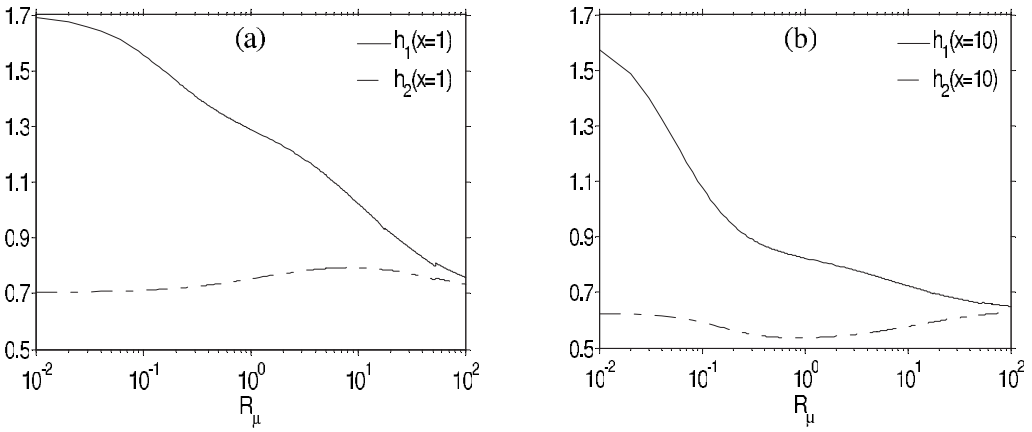

FIG. 3. Dependence of interface height (dash-dotted curve) and free surface height (solid curve) on the viscosity ratio for $\theta=90°$, $\varepsilon=0.1$, $R_H=2$, and Re=100. The heights are plotted at $x=1$ (a) and 10 (b).

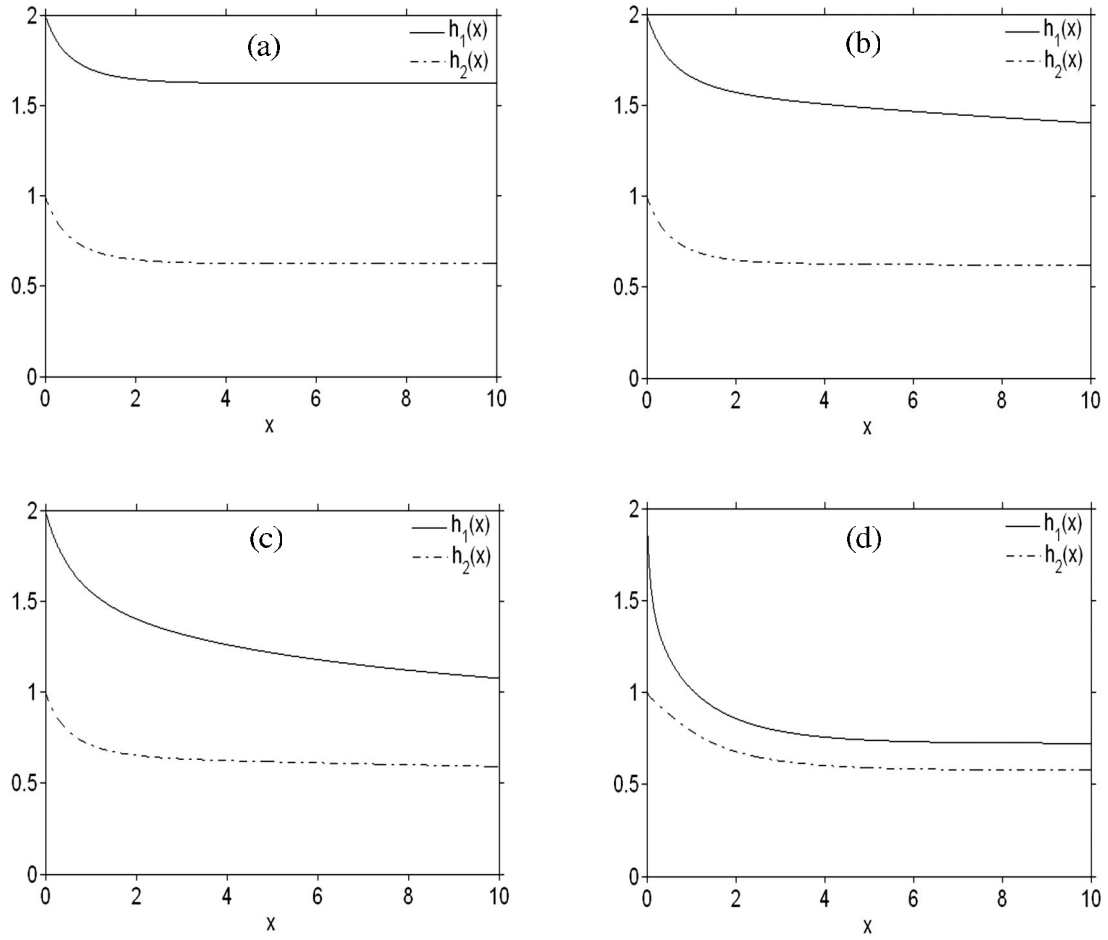

FIG. 4. Effect of viscosity ratio on the interface and free surface profiles, for R_μ=0.001 (a), 0.03 (b), 0.1 (c), and 10 (d), for θ=90°, ε=0.1, R_H=2, and Re=100.

$$2\left(\frac{2\cot\theta}{\mathrm{Re}}-\frac{1}{5h^3}\right)h'=\frac{1}{\mathrm{Re}\,\varepsilon}\left(4-\frac{1}{h^3}\right). \tag{17}$$

Clearly, the right-hand side of Eq. (17) remains positive at inception. In this case, the equation suggests that the film slope changes sign at a critical plate angle given by $\theta_c=\cot^{-1}(\mathrm{Re}/10)$, which in turn reflects the change from film expansion to film contraction at inception.

Figure 6 illustrates typical streamwise velocity profiles for small and large inclination angles. The profiles are given at different but equally distant x locations. The free surface and interface profiles are also shown. Here again $R_\mu=R_\mathrm{H}=2$. Figure 6(a) shows the profiles when gravity is negligible for $\theta=3°$ [see also Figs. 5(a) and 5(b)]. Figure 6(b) displays the profiles for dominant gravity for $\theta=90°$ [see also Figs. 5(c) and 5(d)]. Although both elongational and shear effects are expected to be present, the predominantly elongational character of the flow is evident when gravity is strong, as reflected in the rapid axial gradient of the velocity exhibited in Fig. 6(b). For weak gravity, elongation is particularly strong near inception but rapidly becomes constant because of the uniform expansion rate [see Fig. 6(a)].

The interplay between viscosity and thickness ratios is illustrated in Fig. 7. The heights h_1 and h_2 at $x=10$ are plotted against R_H for typically a small and a large R_μ value. Figure 8 displays the profiles of the free surface and interface for three different R_H values for the same two viscosity ratios as in Fig. 7. In order to investigate the effect of R_H on film heights, this parameter is varied over a fairly broad range, $R_H\in[1,10]$. Note that the limit $R_H\to 1$ corresponds to one-layer film flow. Close to this limit, there is essentially no fluid flowing in the upper layer, which explains the lack of dependence of film height on R_μ [see also Fig. 8(a)]. As R_H increases, the interface height remains relatively unaffected but that of the free surface increases essentially linearly with R_H. The increase in free surface height is clearly depicted in Fig. 7, which reflects weaker gravity. This is also confirmed from the expression of the Froude number in Sec. II, which for dominant thickness ratio gives $\mathrm{Fr}\approx\varepsilon/4\sin\theta R_H\,\mathrm{Re}$. This shows that gravity is weakened for films with large thickness ratio.

B. Flow with dominant surface or interfacial tension

The influence of surface and interfacial tensions is now examined by varying the capillary number Ca and surface-tension ratio R_σ. It is generally found that surface or interfacial tension at even relatively large capillary number can

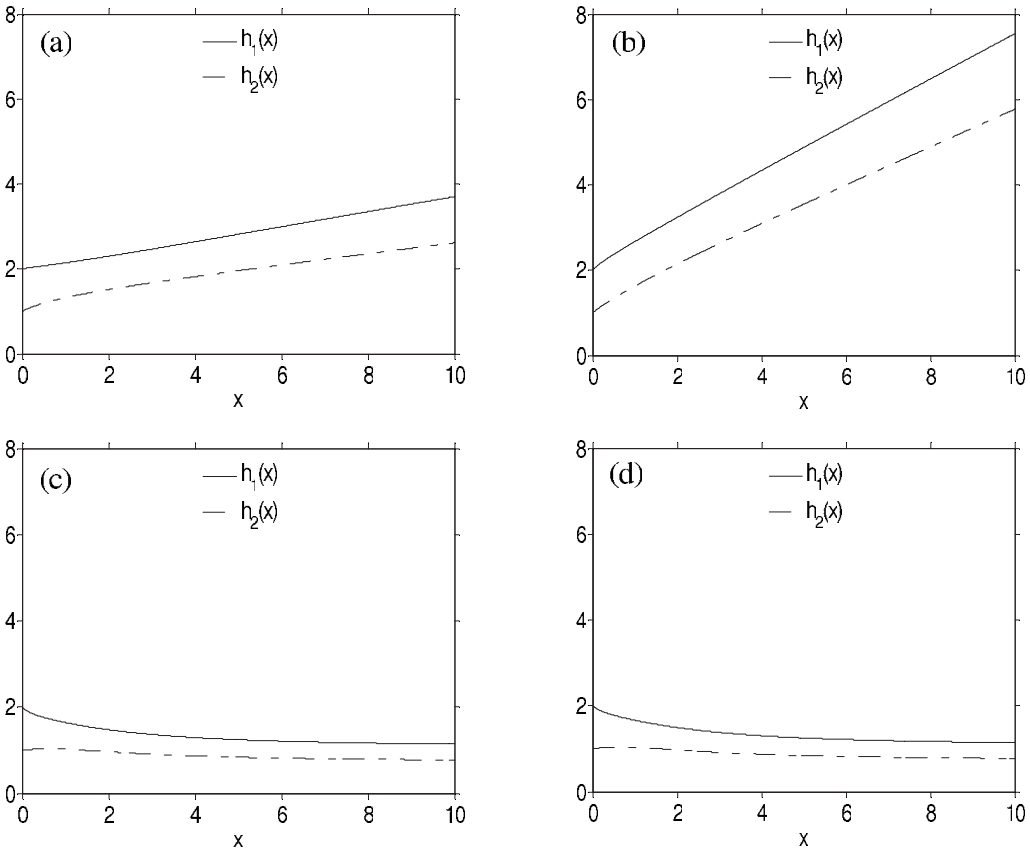

FIG. 5. Effect of viscosity ratio on the interface and free surface profiles, for $\theta=1°$ (a), 3° (b), 30° (c), and 90° (d), for $\varepsilon=0.1$, $R_\mu=2$, $R_H=2$, and Re=100.

have a significant qualitative effect on the flow, although the flow field remains quantitatively close to the flow without surface and interfacial tension. The flow field in the presence of surface and interfacial tension is typically illustrated in Fig. 9 for Ca=0.1, $R_\sigma=1$, and $\varepsilon=0.1$. The film shape and the distributions of the streamwise and depthwise velocity components along the free surface and interface are shown in Figs. 9(a)–9(c), respectively. Note that the film heights in the absence of surface or interfacial tension are the mean heights [see also Fig. 10(b)]. Surface tension is expected to have a stabilizing effect near the origin. The stabilizing effect of surface or interfacial tension is of course due to the weakening of elongational flow (and consequent film flattening) upon flow inception. Further downstream, however, surface or interfacial tension is destabilizing. From the distributions of $h_1(x)$ and $h_2(x)$, it appears that this destabilization is experienced essentially uniformly across the film depth. This uniform response across the film is somewhat expected in the present case since $R_\sigma=1$. However, even in this case, although the modulation amplitude and phase in $h_1(x)$ and $h_2(x)$ are essentially the same, there is significant discrepancy in the behavior of the velocity at the free surface and the interface. There seems to be considerable elongational effect experienced at the free surface compared to the interface as indicated by the higher jumps and drops in $u_1(x,y=h_1)$ compared to $u_2(x,y=h_2)$ in Fig. 9(b). In contrast, Fig. 9(c) shows that the depthwise velocity component at the free surface is essentially the same as that at the interface. Some higher harmonics are present in $v_1(x,y=h_1)$. In general, the amplitude of film modulation grows with streamwise distance, leading to sharp gradients in film shape and flow field.

The level of surface and interfacial tension influences the film shape and flow field significantly. This is illustrated in Fig. 10, which displays the interface and free surface profiles at four different capillary numbers. In the limit $\mathrm{Ca}\to\infty$, one expects to recover the flow in the absence of surface and interfacial tension. This limit is approached with surface or interface modulation exhibiting an increasingly larger wave number and smaller amplitude as Ca increases. Note that the limit of infinite Ca leads to a singularity and consequently to the large wave number. At large capillary number (Ca=1), Fig. 10(a) shows that both $h_1(x)$ and $h_2(x)$ remain wavy, but the profiles display a similar *mean* behavior to that corresponding to the flow with negligible surface and interfacial tension. This is further illustrated in Fig. 10(b) for Ca=0.1. The curves corresponding to the flow in the absence of surface and interfacial tension are added in the figure for reference. As surface tension effects become stronger, the modulation wavelength and amplitude increase. This behavior was also predicted by Benjamin [31] for one-layer flow, who showed that, for different values of the Reynolds number, increasing surface tension results in a decrease in wave number (an increase in wavelength). Figure 10(b) shows that only the amplitude increases with position, reflecting an obvious destabilization of the film downstream. As Ca decreases further, the instability is swept further downstream

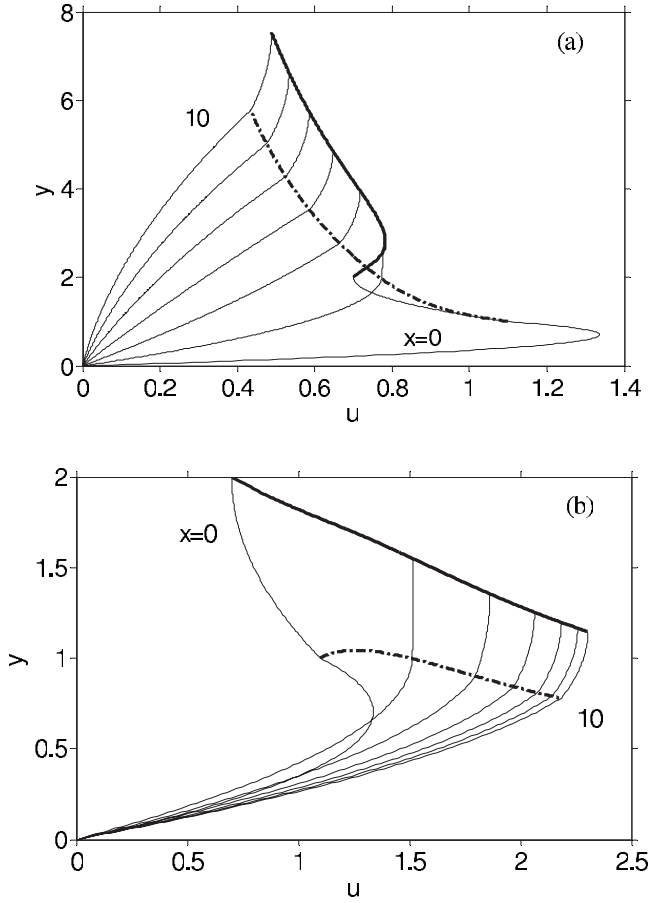

FIG. 6. Streamwise velocity profiles for $\varepsilon=0.1$, $R_\mu=2$, $R_H=2$, and Re=100. Free surface (thick solid curve) and interface (thick dash-dotted curve) are also shown. (a) and (b) illustrate the velocity profiles at different x locations, from $x=0$ to 10 in equal steps for $\theta=3°$ and $\theta=90°$, respectively.

[Fig. 10(c)], but eventually disappears altogether when Ca decreases below a critical value [Fig. 10(d)]. This apparent convective instability is related to the onset of ribbing lines in three-dimensional one-layer flow [32]. Pitts and Greiller [33] determined the capillary number at which the coating meniscus between linearly diverging surfaces becomes unstable. They found that the critical capillary number increases with angle of divergence. The present flow is inertia dominated, which involves a film with small angle of divergence; the film tends to move downstream instead of accumulating near the origin. Accordingly, surface- or interface-induced modulation is expected to disappear at relatively small Ca.

The influence of gravity on the two-layer flow in the presence of surface and interfacial tension is illustrated in Fig. 11, where the effect of the plate slope on the interface and free surface profiles is displayed. It is generally observed that, as the driving (gravity) force decreases, the free surface and interface modulation amplitude increases, resulting from the increasingly dominating surface tension effect. This behavior is in agreement with the predictions of Parau *et al.* [34], who examined the effect of capillarity and gravity on solitary waves in deep media.

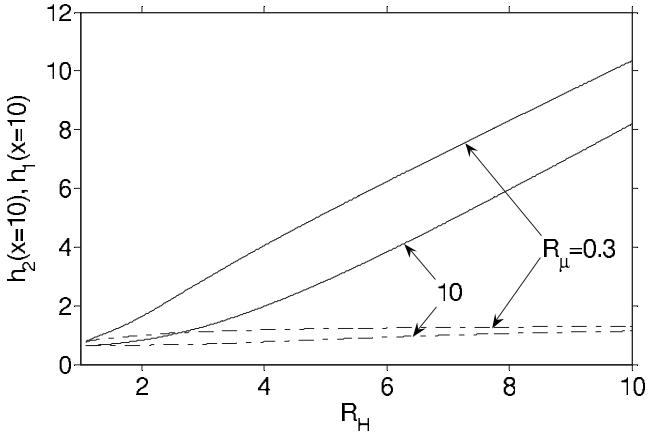

FIG. 7. Dependence of free surface (solid curves) and interface (dash-dotted curves) heights on film thickness ratio, for small and large viscosity ratios $R_\mu=0.3$ and 10, respectively, for $\theta=90°$, $\varepsilon=0.1$, and Re=100.

Finally, the interplay between free surface and interfacial tensions is examined by varying the surface tension ratio at relatively small capillary number ($\mathrm{Ca}=10^{-5}$), and is illustrated in Fig. 12. Here, the free surface and interface profiles are shown at $R_\sigma=0.05$, 1, and 10, and the other parameters are $R_\mu=2$, $R_H=2$, Re=100, and $\varepsilon=0.1$. A relatively large free surface tension tends generally to stabilize the film and reduce the surface curvature (see curves corresponding to $R_\sigma=10$). In this case, the interface exhibits pronounced waviness. On the other hand, larger interfacial tension has a destabilizing effect on the film surface. In this case, the modulation appears to be particularly enhanced in wave number at the free surface. The interface tends to display delayed modulation, but with relatively less pronounced amplitude (see curves corresponding to $R_\sigma=0.05$). At large R_σ, the interface modulation amplitude is large enough for it to penetrate through the free surface at some location downstream.

C. One-layer flow

The emergence of surface modulation is an important issue, which can be further understood by examining the simpler one-layer steady film flow. In this case, the equation governing the film thickness $h(x)$ reduces to (see Appendix C)

$$\delta h''' = \left(\varepsilon\frac{\cos\theta}{\mathrm{Fr}} - \frac{6}{5h^3}\right)h' + \frac{3}{\mathrm{Re}\,\varepsilon h^3} - \frac{\sin\theta}{\mathrm{Fr}}, \qquad (18)$$

where $\delta=\varepsilon^2/\mathrm{Re\,Ca}$. The equation above must be solved subject to the boundary conditions $h(0)=1$, $h'(0)=0$, $h''(0)=0$. For large δ, a regular perturbation expansion can be carried out in $1/\delta$, for $\theta=90°$, namely,

$$h(x) = 1 + \left(\frac{3}{\mathrm{Re}\,\varepsilon} - \frac{1}{\mathrm{Fr}}\right)\frac{x^3}{6}\left(\frac{1}{\delta}\right) - \left\{\left(\frac{3}{\mathrm{Re}\,\varepsilon} - \frac{1}{\mathrm{Fr}}\right)\left[\left(\frac{3}{\mathrm{Re}\,\varepsilon} - \frac{1}{\mathrm{Fr}}\right) + \frac{1}{\mathrm{Fr}}\right]\frac{x^6}{240} + \left(\frac{3}{\mathrm{Re}\,\varepsilon} - \frac{1}{\mathrm{Fr}}\right)\frac{x^5}{100}\right\}\left(\frac{1}{\delta}\right)^2 + O\left(\frac{1}{\delta}\right)^3. \qquad (19)$$

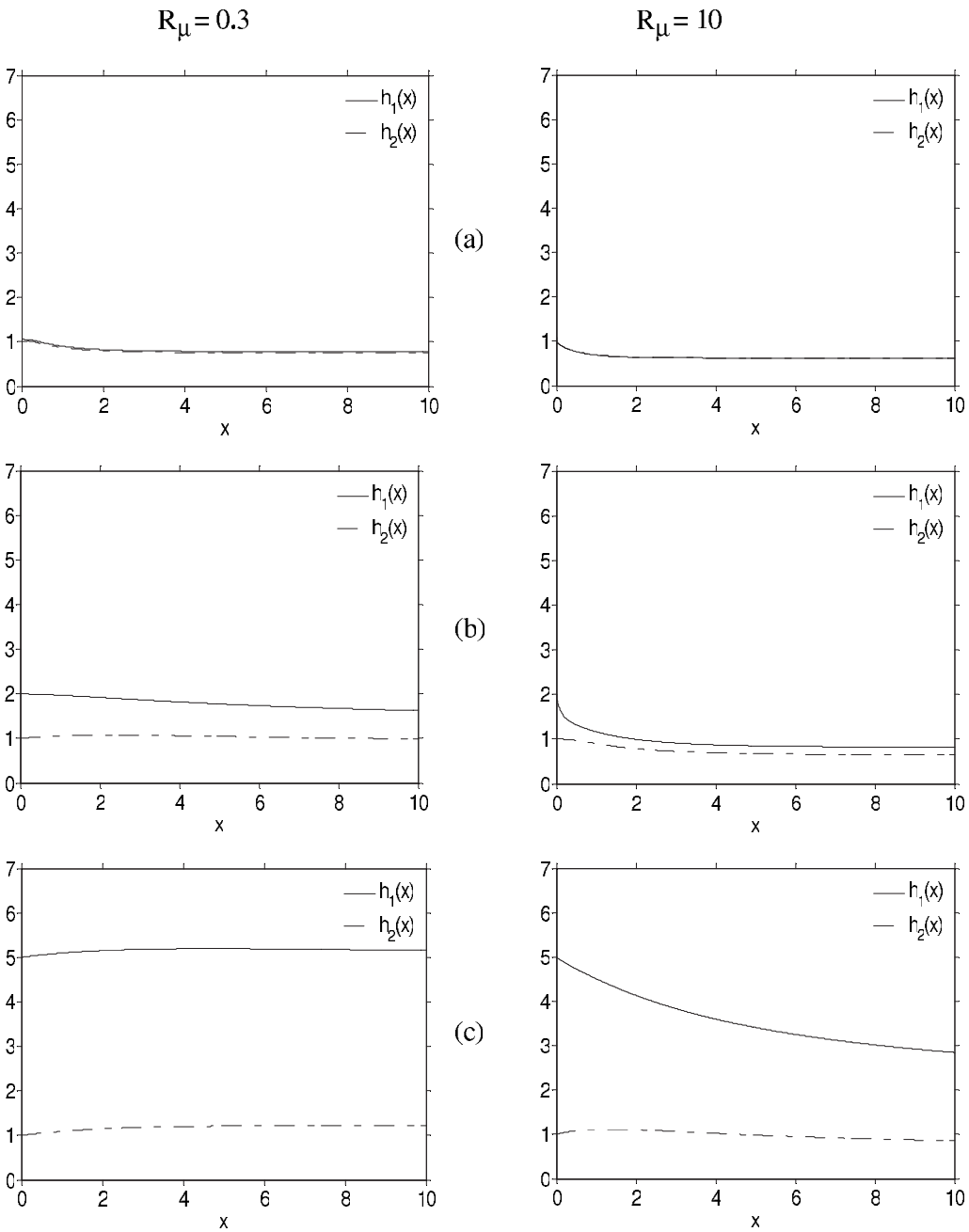

FIG. 8. Effect of film thickness ratio on the free surface and interface profiles for small and large viscosity ratio, R_μ=0.3 and 10, respectively, and R_H=1.1 (a), 2 (b), and 5 (c), for θ=90°, ε=0.1, and Re=100.

Clearly, this solution, although approximate, suggests that the film growth is strictly monotonic in the presence of strong surface tension. This behavior is also in agreement with the current numerical findings for two-layer flow [see Fig. 10(d)] where the modulation is significantly attenuated. On the other hand, for small δ, Eq. (18) exhibits a *global* breakdown as opposed to the *local* breakdown typically encountered in boundary-layer problems. This fact is intuitively expected given the absence of the second derivative in Eq. (18), and the rapid oscillation exhibited at small δ for two-layer flow [see Figs. 10(a) and 10(b)]. Nevertheless, an approximate solution can still be sought using singular perturbation expansion in the neighborhood of x=0. A suitable rescaling in this case is given by $X=x/\sqrt{\delta}$, $H=h$, which leads to the following equation for H:

$$H^3H''' + \frac{6}{5}H' + \frac{H^3}{\mathrm{Fr}}\sqrt{\delta} - \frac{3\sqrt{\delta}}{\mathrm{Re}\,\varepsilon} = 0. \tag{20}$$

This equation is now solved using a regular perturbation expansion,

$$h(x) = 1 + \frac{5}{6}\left(\frac{3}{\mathrm{Re}\,\varepsilon} - \frac{1}{\mathrm{Fr}}\right)x - \left(\frac{5}{6}\right)^{1.5} \times \left(\frac{3}{\mathrm{Re}\,\varepsilon} - \frac{1}{\mathrm{Fr}}\right)\sin\left(\sqrt{\frac{6}{5}}\frac{x}{\sqrt{\delta}}\right)\sqrt{\delta} + c\,\delta. \tag{21}$$

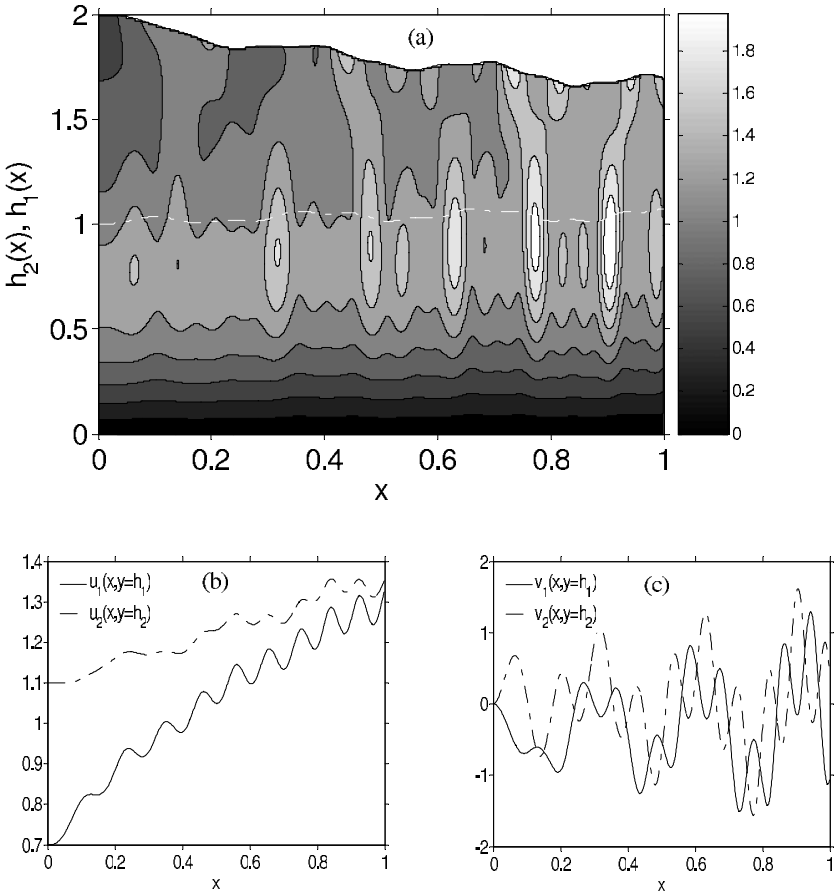

FIG. 9. Typical two-layer film flow for $\theta=90°$, $\varepsilon=0.1$, $R_\mu=2$, $R_H=2$, $R_\sigma=1$, Ca=0.1, and Re =100. (a) shows the free surface (solid curve) and interface (dash-dotted curve) heights as well as the velocity magnitude contours. (b) and (c) display the dependence of horizontal and vertical velocity components, respectively, at both interface (dash-dotted curve) and free surface (solid curve) on x.

In this case, the solution clearly hints at an oscillatory behavior which confirms the current numerical findings for two-layer flow [see Figs. 10(a) and 10(b)]. In addition, it is not difficult to infer from solution (21) that, while the amplitude of oscillation of the streamwise velocity at the free surface is $O(\sqrt{\delta})$, that of the transverse component is $O(1)$. This behavior correlates closely with the one depicted in Figs. 10(b) and 10(c). Figure 13 displays the profile of the free surface for typically large [Fig. 13(a)] and small [Fig. 13(b)] surface tension, along with a comparison between approximate and numerical solutions. For large surface tension, agreement between the two solutions is found over a long distance from the origin, far beyond the region of validity of the regular perturbation expansion. In contrast, for small surface tension, the two solutions agree only over a small distance. The wavy behavior of the free surface shown in Fig. 13(b) may be qualitatively compared to the numerical results given by Parau *et al.* [34] for inviscid three-dimensional gravity-capillary solitary waves. They found that the oscillatory wave amplitude decreases as surface tension decreases. This behavior is confirmed here in Fig. 14, where the wave amplitude ζ is plotted against Ca for different angles of inclination, at a location sufficiently far from inception where the flow is fairly settled (in this case $x=2$). As is evident from Fig. 14, at small Ca, the wave amplitude tends to decreases rapidly as surface tension diminishes, but eventually becomes insensitive to the surface-tension effect at large Ca. Note that this behavior is also predicted for two-layer film flow (see Fig. 10). The inset in Fig. 14 shows a log-log plot, which in turn reveals a simple general dependence of the wave amplitude on surface tension, namely, $\zeta \sim \mathrm{Ca}^{-0.3}$. Interestingly, there is essentially no dependence on the angle of inclination.

The possibility of conducting experiments for two-layer flow is limited by the complex nature of the problem. However, there are numerous experiments carried out on the one-layer film flow, with results that can still be generalized to two-layer flow under certain circumstances. For instance, Pierson and Whitaker [35] examined the wavy structure of water flowing down a vertical plane experimentally and numerically. They showed that when the Reynolds number increases, the wavelength of surface waves decreases, which results in an increase in wave number α. This phenomenon can also be seen from Fig. 15 where the free surface profile is plotted for different Reynolds numbers using the properties of water. Figure 16 depicts the dependence of the wave number defined as $\alpha=2\pi h_m/\lambda$, where h_m is the mean film height and λ is the wavelength, on Re. The data, which are based on the profiles shown in Fig. 15, suggest a linear response, which is reflected in the results of Pierson and Whitaker [35] for large Reynolds number.

IV. CONCLUSION

Two-layer thin-film flow over an inclined stationary solid substrate is examined in this study. The film is assumed to emerge out of a channel and flow over a straight plate. The fluid density is assumed to be uniform over the flow domain,

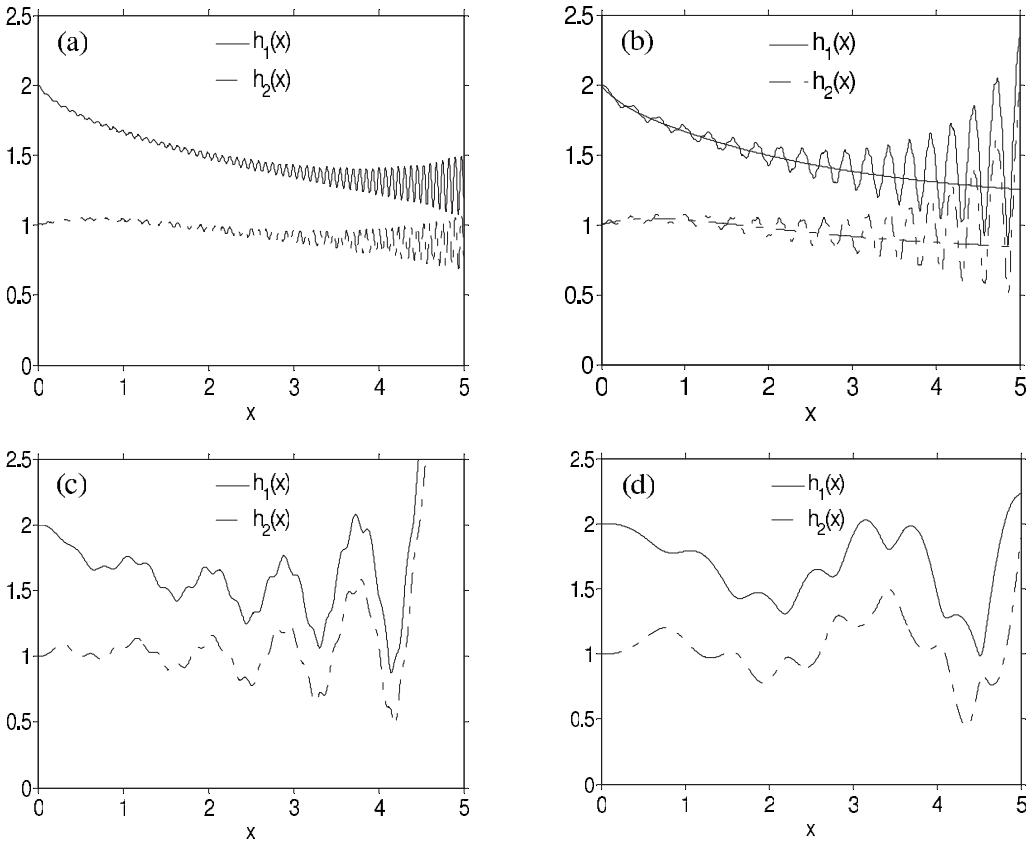

FIG. 10. Effect of surface tension on the interface and free surface profiles. (a), (b), (c), and (d) correspond to Ca=1, 0.1, 0.01, and 0.001, respectively, for $\theta=90°$, $\varepsilon=0.1$, $R_\mu=2$, $R_H=2$, $R_\sigma=1$, and Re=100. In addition, curves corresponding to flow in the absence of surface and interfacial tension are also added to (b) for reference.

but the viscosity and surface tension in each layer can be different. The influence of flow parameters, such as the viscosity ratio R_μ, film thickness ratio at inception R_H, plate angle θ, and surface-to-interfacial tension ratio R_σ, is investigated. Depending upon the level of the surface-tension effect, a regular and singular perturbation solution near inception can be obtained for one-layer film flow, and close agreement is found between the numerical and approximate solutions. Furthermore, for one-layer film flow down a vertical wall, the effect of Reynolds number Re on wave number is also studied, indicating that the surface wave number increases linearly with inertia.

The viscosity ratio and film thickness ratio at inception have a strong influence on the film thickness downstream. In the absence of surface and interfacial tension, the film thickens with increasing R_H and decreases in height with increasing R_μ. A jump in height occurs at some critical viscosity ratio further downstream. The free surface and interface tend to become thinner as the gravity effect becomes stronger.

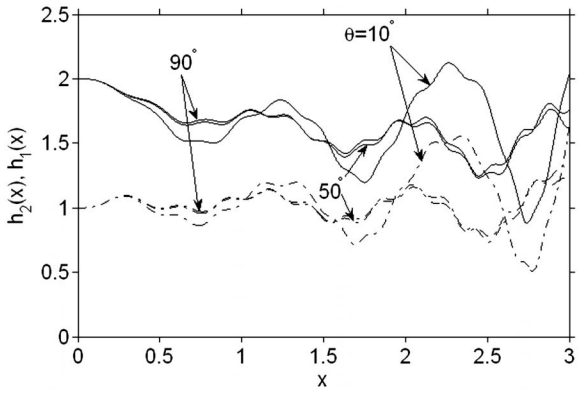

FIG. 11. Effect of plate slope on the interface and free surface profiles for different plate angles $\theta=90°$, 50°, and 10° for $\varepsilon=0.1$, $R_\mu=2$, $R_H=2$, $R_\sigma=1$, Ca=0.01, and Re=100.

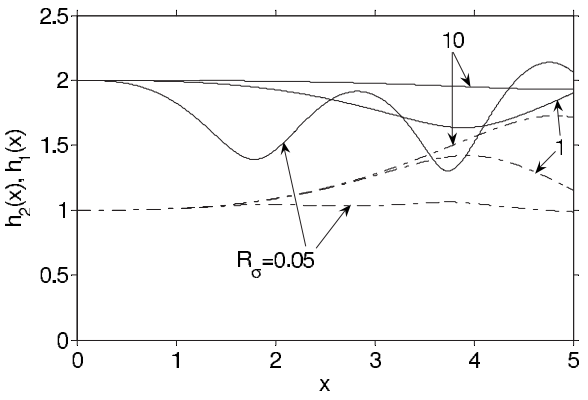

FIG. 12. Effect of surface tension ratio on the free surface (solid curves) and interface (dash-dotted curves) profiles, corresponding to $R_\sigma=0.05$, 1, and 10. Other parameters are $\theta=90°$, $\varepsilon=0.1$, $R_\mu=2$, $R_H=2$, Ca=10^{-5}, and Re=100.

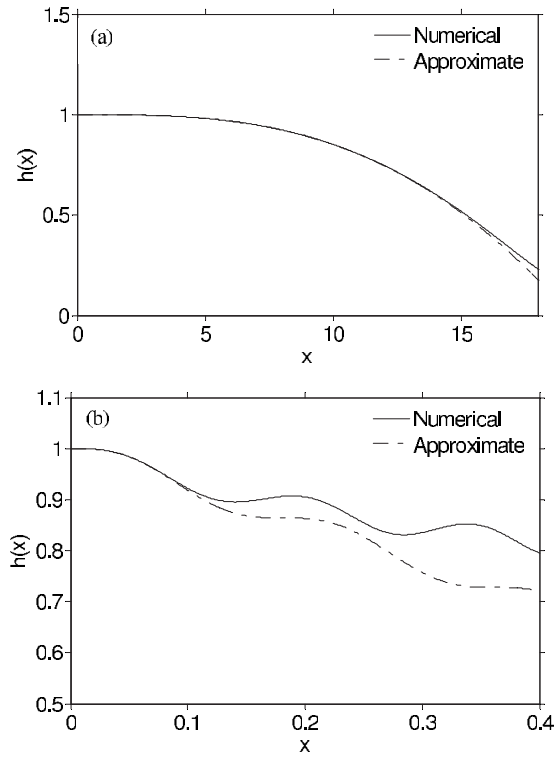

FIG. 13. Free surface profiles for one-layer film flow. Comparison between numerical and approximate solutions for typical (a) large surface tension $\delta=10^3$ and (b) small surface tension $\delta=10^{-3}$ for $\theta=90°$, $\varepsilon=0.1$, Re=100.

There is a change from film expansion to film contraction at inception as the gravity effect increases. For one-layer flow, the film slope changes sign at a critical plate angle $\theta_c=\cot^{-1}(\mathrm{Re}/10)$. The surface or interfacial tension at even relatively large capillary number is found to have a significant qualitative effect on the flow, although the flow field remains quantitatively close to the flow without surface and interfacial tension. Despite the stabilizing effect of surface tension near inception, surface modulation appears downstream, which increases in wavelength and amplitude as the surface-tension effect becomes stronger, and finally disappears at relatively small Ca. The free surface modulation tends to diminish with increase in R_σ. Finally, the effect of capillary and Reynolds numbers on the wave amplitude and wave number is investigated for the simpler one-layer case, and the results show good agreement with existing theory and experiment.

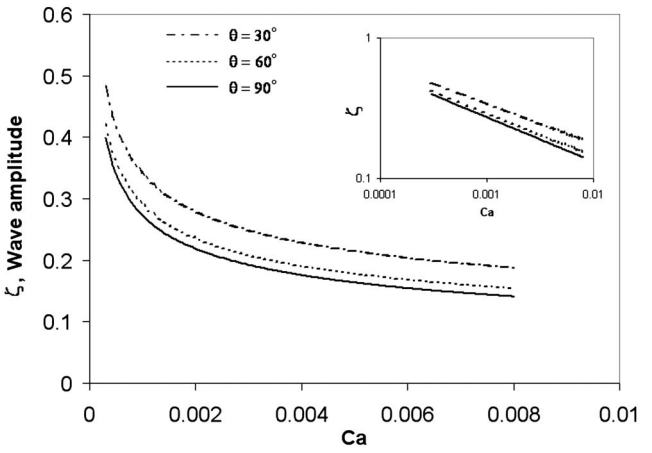

FIG. 14. Wave amplitude versus Ca for $\varepsilon=0.1$ and Re=100 for different plate angles. Inset shows log-log plots.

APPENDIX A: DYNAMIC CONDITIONS

Cast in dimensionless form, the explicit forms for the dynamic condition in the normal and tangential directions at the free surface ($y=h_1$) are given by

$$\frac{2\varepsilon^2}{1+\varepsilon^2\left(\frac{\partial h_1}{\partial x}\right)^2}\left[-\varepsilon^2\left(\frac{\partial h_1}{\partial x}\right)^2\frac{\partial u_1}{\partial x}+\frac{\partial h_1}{\partial x}\frac{\partial u_1}{\partial y}+\varepsilon^2\frac{\partial h_1}{\partial x}\frac{\partial v_1}{\partial x}-\frac{\partial v_1}{\partial y}\right]+p_1=\frac{-\frac{R_\sigma\varepsilon^3}{\mathrm{Ca}}\frac{\partial^2 h_1}{\partial x^2}}{\left[1+\varepsilon^2\left(\frac{\partial h_1}{\partial x}\right)^2\right]^{3/2}}, \tag{A1}$$

$$-\mu_1\left(\frac{\partial u_1}{\partial y}-\varepsilon^2\frac{\partial v_1}{\partial x}\right)\left[1-\varepsilon^2\left(\frac{\partial h_1}{\partial x}\right)^2\right]+2\mu_1\varepsilon\frac{\partial h_1}{\partial x}\left(\varepsilon\frac{\partial u_1}{\partial x}-\varepsilon\frac{\partial v_1}{\partial y}\right)=0. \tag{A2}$$

Similarly, the dynamic conditions in the normal and tangential directions at the interface ($y=h_2$) are

$$\frac{2\varepsilon^2}{1+\varepsilon^2\left(\frac{\partial h_2}{\partial x}\right)^2}\left[-\varepsilon^2\left(\frac{\partial h_2}{\partial x}\right)^2\frac{\partial u_2}{\partial x}+\frac{\partial h_2}{\partial x}\frac{\partial u_2}{\partial y}+\varepsilon^2\frac{\partial h_2}{\partial x}\frac{\partial v_2}{\partial x}-\frac{\partial v_2}{\partial y}\right]+p_2$$

$$+\frac{2R_\mu\varepsilon^2}{1+\varepsilon^2\left(\frac{\partial h_2}{\partial x}\right)^2}\left[\varepsilon^2\left(\frac{\partial h_2}{\partial x}\right)^2\frac{\partial u_1}{\partial x}-\frac{\partial h_2}{\partial x}\frac{\partial u_1}{\partial y}-\varepsilon^2\frac{\partial h_2}{\partial x}\frac{\partial v_1}{\partial x}+\frac{\partial v_1}{\partial y}\right]-p_1=\frac{-\frac{\varepsilon^3}{\mathrm{Ca}}\frac{\partial^2 h_2}{\partial x^2}}{\left[1+\varepsilon^2\left(\frac{\partial h_2}{\partial x}\right)^2\right]^{3/2}}, \tag{A3}$$

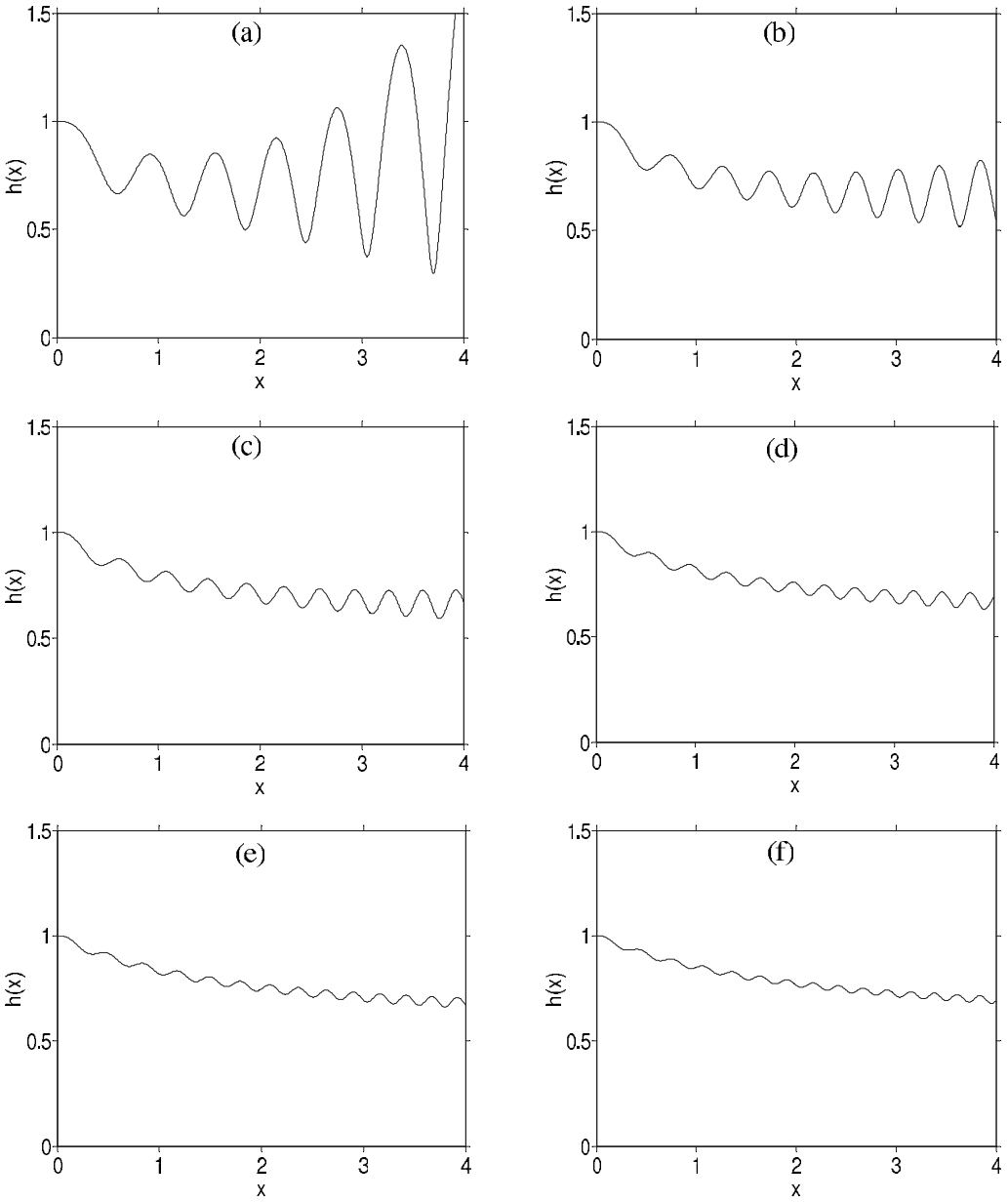

FIG. 15. Effect of Reynolds number on the free surface profile for Re=100 (a), 150 (b), 200 (c), 250 (d), 300 (e), and 350 (f) for $\theta=90°$ and $\varepsilon=0.1$ using water properties.

$$\mu_1\left(\frac{\partial u_1}{\partial y}+\varepsilon^2\frac{\partial v_1}{\partial x}\right)\left[1-\varepsilon^2\left(\frac{\partial h_2}{\partial x}\right)^2\right]-2\mu_1\varepsilon\frac{\partial h_2}{\partial x}\left(\varepsilon\frac{\partial u_1}{\partial x}+\varepsilon\frac{\partial v_1}{\partial y}\right)-\mu_2\left(\frac{\partial u_2}{\partial y}-\varepsilon^2\frac{\partial v_2}{\partial x}\right)\left[1-\varepsilon^2\left(\frac{\partial h_2}{\partial x}\right)^2\right]+2\mu_2\varepsilon\frac{\partial h_2}{\partial x}\left(\varepsilon\frac{\partial u_2}{\partial x}-\varepsilon\frac{\partial v_2}{\partial y}\right)=0. \tag{A4}$$

When higher-order terms in ε are neglected, the dynamic conditions reduce to expressions (4) and (5).

Integrating the y-momentum equation in (2) of the upper layer and in (3) of the lower layer with respect to y leads to the following expressions for the pressure in each layer:

$$p_1=-\mathrm{Re}\,\varepsilon^2\frac{\cos\theta}{\mathrm{Fr}}y+C_1(x), \tag{A5}$$

$$p_2=-\mathrm{Re}\,\varepsilon^2\frac{\cos\theta}{\mathrm{Fr}}y+C_2(x), \tag{A6}$$

where $C_1(x)$ and $C_2(x)$ are determined by using (4) and (5), to give

$$C_1(x)=\mathrm{Re}\,\varepsilon^2\frac{\cos\theta}{\mathrm{Fr}}h_1-\frac{R_\sigma\varepsilon^3}{\mathrm{Ca}}h_1'', \tag{A7}$$

$$C_2(x)=-\frac{\varepsilon^3}{\mathrm{Ca}}h_2''-\mathrm{Re}\,\varepsilon^2\frac{\cos\theta}{\mathrm{Fr}}h_2+\mathrm{Re}\,\varepsilon^2\frac{\cos\theta}{\mathrm{Fr}}h_1-\frac{R_\sigma\varepsilon^3}{\mathrm{Ca}}h_1''+\mathrm{Re}\,\varepsilon^2\frac{\cos\theta}{\mathrm{Fr}}h_2, \tag{A8}$$

which in turn lead to Eqs. (12).

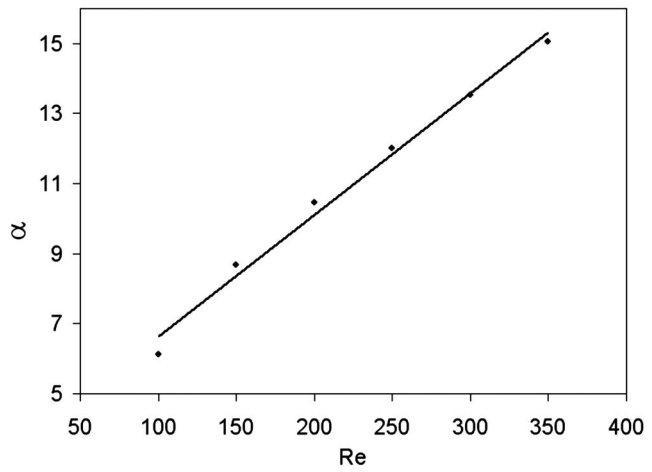

FIG. 16. Wave number versus Re (same parameter values as in Fig. 15).

APPENDIX B: COEFFICIENTS IN EQ. (15)

The coefficients are

$$P_1 = \frac{2}{3}h_1^3 + \left(R_\mu - \frac{2}{3}\right)h_2^3 + (-3R_\mu + 2)h_1h_2^2 + 2(R_\mu - 1)h_2h_1^2,$$

$$Q_1 = \left(h_1 - \frac{h_2}{3}\right)h_2^2,$$

$$R_1 = 2A_1h_1^2 + (-4 + 4R_\mu)A_1h_1h_2 + [A_2 + (-3R_\mu + 1)A_1]h_2^2,$$

$$S_1 = (h_2 - h_1)(2A_1h_1 - 2R_\mu A_1h_1 - 2A_1h_2 - 2A_2h_2 + 4R_\mu A_1h_2) - \frac{h_2^2}{2}(2R_\mu A_1 - 2A_2),$$

$$P_2 = R_\mu h_2^2(h_2 - h_1),$$

$$Q_2 = -\frac{2}{3}h_2^3,$$

$$R_2 = -R_\mu A_1h_2^2,$$

$$S_2 = 3R_\mu A_1h_2^2 - 2R_\mu A_1h_1h_2 - 2A_2h_2^2,$$

$$P_3 = \frac{1}{3}(2R_\mu^2h_2^5A_1 - 4R_\mu^2A_1h_1h_2^4 + 2R_\mu^2A_1h_1^2h_2^3 - 2R_\mu A_2h_2^5 + 2R_\mu A_2h_1h_2^4),$$

$$Q_3 = \frac{1}{3}\left(\frac{6}{5}A_2h_2^5 - R_\mu A_1h_2^5 + R_\mu A_1h_1h_2^4\right),$$

$$R_3 = \frac{1}{3}(2R_\mu^2A_1^2h_1h_2^3 - 2R_\mu^2A_1^2h_2^4 + 2R_\mu A_1A_2h_2^4) + \varepsilon\frac{\cos\theta}{\mathrm{Fr}}h_2,$$

$$S_3 = \frac{1}{3}(2R_\mu^2A_1^2h_2^4 - 4R_\mu A_1A_2h_2^4 - 2R_\mu^2A_1^2h_1h_2^3 + 2R_\mu A_1A_2h_1h_2^3 + 2A_2^2h_2^4),$$

$$P_4 = (h_1^5 - h_2^5)\frac{A_1}{15} - \frac{(h_1^4 - h_2^4)}{3}A_1h_1 + 2(h_1 - h_2)A_1h_2^2h_1\left[h_1(1 - R_\mu) + h_2\left(-\frac{1}{3} + R_\mu\right)\right] + \frac{(h_1^3 - h_2^3)}{3}[2(1 - R_\mu)A_1h_1h_2 - h_2^2A_2 + (2R_\mu - 1)A_1h_2^2 + 2A_1h_1^2] + (h_1^2 - h_2^2)\left[\left(\frac{1}{3} - R_\mu\right)A_1h_2^3 + 2(R_\mu - 1)A_1h_1^2h_2 - R_\mu A_1h_1h_2^2 + h_2^2A_2h_1\right] + h_2[2(1 - R_\mu)h_1 + (-1 + 2R_\mu)h_2]\left[A_1h_2^3\left(\frac{1}{3} - 2R_\mu\right) - \frac{1}{3}A_1h_1^3 + A_1h_2h_1^2(1 - 2R_\mu) + A_1h_1h_2^2(-1 + 4R_\mu) - h_2^2A_2h_1 + h_2^2A_2h_2\right],$$

$$Q_4 = (-h_2^2)\left(\frac{(h_2^3 - h_1^3)A_1}{3} + (h_1^2 - h_2^2)A_1h_2 + (h_1 - h_2)(-2R_\mu A_1h_1h_2 + (-1 + 2R_\mu)A_1h_2^2 - h_2^2A_2)\right) - \frac{4A_1h_1h_2^3}{3}(h_1 - h_2) + \frac{2A_1h_2^3}{3}(h_1^2 - h_2^2),$$

$$R_4 = (-A_1)\left(-\frac{2A_1h_1}{3}(h_1^3 - h_2^3) + (h_1^2 - h_2^2)[2A_1h_1h_2(1 - R_\mu) - h_2^2A_2 + 2R_\mu A_1h_2^2] - 2A_1h_1h_2^2(h_1 - h_2)\right) + 2A_1h_2(1 - R_\mu)\left(\frac{A_1}{3}(h_2^3 - h_1^3) + (h_1^2 - h_2^2)A_1h_2 + (h_1 - h_2)[-2R_\mu A_1h_1h_2 - h_2^2A_2 + (2R_\mu - 1)A_1h_2^2]\right) + R_\mu A_1[A_1h_2^2(h_1^2 - h_2^2) - 2A_1h_1h_2^2(h_1 - h_2)] + \varepsilon\frac{\cos\theta}{\mathrm{Fr}}(h_1 - h_2),$$

$$S_4 = \left(\frac{(h_2^3 - h_1^3)A_1}{3} + (h_1^2 - h_2^2)A_1 h_2 + (h_1 - h_2)[-2R_\mu A_1 h_1 h_2 - h_2^2 A_2 + (2R_\mu - 1)A_1 h_2^2] \right)[2A_1 h_1(1 - R_\mu)$$
$$- 2A_2 h_2 + 2(-1 + 2R_\mu)A_1 h_2] - [A_1 h_2^2(h_1^2 - h_2^2) - 2A_1 h_1(h_1 - h_2)h_2^2](R_\mu A_1 - A_2).$$

APPENDIX C: GOVERNING EQUATION FOR ONE-LAYER THIN-FILM FLOW

In the limit $h_1 \to h_2$ $(A_1 \to A_2)$, the first equation in (15) reads

$$(P_1 + Q_1)A_2' + (R_1 + S_1)h_2' = 0. \tag{C1}$$

Substituting for the coefficients P_1, Q_1, R_1, and S_1 into (C1) gives

$$(h_2^3 A_2)'(h)' = 0 \tag{C2}$$

or

$$A_2 = \frac{C}{h_2^3} \tag{C3}$$

where C is a constant. On the other hand, from Eq. (14), A_2 can be expressed as the following:

$$A_2 = \frac{3}{2h_2^2}(R_\mu A_1 h_2^2 - R_\mu A_1 h_1 h_2 - \bar{u}_2).$$

In this case, and at the origin, A_2 can be rewritten as

$$A_2(x = 0) = -\frac{3\bar{u}_{02}}{2h_{02}^2}, \tag{C4}$$

where $\bar{u}_{02}$, the dimensionless mean velocity at the origin, and h_{02}, the dimensionless height at the inception, are equal to unity; so $A_2 = -3/2$ at $x = 0$. Finally Eq. (C3) gives $C = -3/2$.

Now let us consider the third equation in (15),

$$P_3 A_1' + Q_3 A_2' + R_3 h_1' + S_3 h_2' = \frac{2A_2 h_2}{\mathrm{Re}\,\varepsilon} + \frac{\sin\theta}{\mathrm{Fr}} h_2 + \frac{\varepsilon^2}{\mathrm{Re\,Ca}} h_2 (h_2''' + R_\sigma h_1''').$$

Note that $h_1 = h_2$, $A_1 = A_2 = -3/2h_2^3$, and $R_\sigma = 0$. After simplification, the governing equation for one-layer thin-film flow height can be expressed as

$$\delta h''' = \left(\varepsilon \frac{\cos\theta}{\mathrm{Fr}} - \frac{6}{5h^3} \right) h' + \frac{3}{\mathrm{Re}\,\varepsilon h^3} - \frac{\sin\theta}{\mathrm{Fr}}, \tag{C5}$$

where $\delta = \varepsilon^2/\mathrm{Re\,Ca}$. In the absence of surface tension, Eq. (C5) becomes

$$\left(\varepsilon \frac{\cos\theta}{\mathrm{Fr}} - \frac{6}{5h^3} \right) h' = -\frac{3}{\mathrm{Re}\,\varepsilon h^3} + \frac{\sin\theta}{\mathrm{Fr}} \tag{C6}$$

[1] A. Oron, S. H. Davis, and S. G. Bankoff, Rev. Mod. Phys. **69**, 931 (1997).
[2] R. E. Khayat and S. Welke, Phys. Fluids **13**, 355 (2001).
[3] R. E. Khayat and K. Kim, Phys. Fluids **14**, 4448 (2002).
[4] E. J. Watson, J. Fluid Mech. **20**, 481 (1964).
[5] S. F. Kistler and P. M. Schweizer, *Liquid Film Coating* (Chapman and Hall, London, 1997).
[6] R. G. Larson, Rheol. Acta **31**, 213 (1992).
[7] T. G. Myers, Phys. Rev. E **72**, 066302 (2005).
[8] R. R. Gorla and L. W. Byrd, J. Fluids Eng. **121**, 651 (1999).
[9] S. Kalliadasis, C. Bielarz, and G. M. Homsy, Phys. Fluids **12**, 1889 (2000).
[10] L. E. Stillwagon and R. G. Larson, J. Appl. Phys. **63**, 5251 (1988).
[11] L. E. Stillwagon and R. G. Larson, Phys. Fluids A **2**, 1937 (1990).
[12] O. Takeshi, Phys. Fluids **11**, 3247 (1999).
[13] V. Y. Shkadov, Izv. Akad. Nauk SSSR, Mekh. Zhidk. Gaza **1**, 43 (1967).
[14] S. V. Alekseenko, V. E. Nakoryakov, and B. G. Pokusaev, AIChE J. **31**, 1446 (1985).
[15] K. J. Ruschak and S. J. Weinstein, J. Fluids Eng. **121**, 673 (1999).
[16] A. Costa and G. Macedonio, Geophys. Res. Lett. **32**, L05304 (2005).
[17] W. J. Schrenk and T. Alfrey, Jr., in *Coextruded Multi-Layer Polymer Films and Sheets, in Polymer Blends*, edited by D. R. Paul and N. Seymour (Academic Press, New York, 1978), Vol. 2, p. 129.
[18] J. L. White, R. C. Ufford, K. R. Dharod, and R. L. Price, J. Appl. Polym. Sci. **16**, 1313 (1972).
[19] T. C. Yu and C. D. Han, J. Appl. Polym. Sci. **17**, 1203 (1973).
[20] C. D. Han and Y. W. Kim, J. Appl. Polym. Sci. **20**, 2609 (1976).
[21] J. H. Southern and R. L. Ballman, J. Appl. Polym. Sci. **20**, 175 (1973).
[22] N. R. Anturkar, T. C. Papanastasiou, and J. O. Wilkes, Chem. Eng. Sci. **45**, 3271 (1990).
[23] D. Joseph, M. Renardy, and Y. Renardy, J. Fluid Mech. **141**, 309 (1984).
[24] A. P. Hooper and R. Grimshaw, Phys. Fluids **28**, 37 (1985).
[25] D. S. Loewenherz and C. J. Lawrence, Phys. Fluids A **1**, 1686 (1989).
[26] C. Pozrikidis, J. Fluid Mech. **371**, 345 (1998).
[27] J. Lee and C. C. Mei, J. Fluid Mech. **307**, 191 (1996).
[28] R. A. Behrens, M. J. Crochet, C. D. Denson, and Metzner.

AIChE J.. **33**, 1178 (1987).
[29] W. Y. Jiang, B. Helenbrook, and S. P. Lin, Phys. Fluids **16**, 652 (2004).
[30] L. E. Reichl, *A Modern Course in Statistical Physics* (University of Texas Press, Austin, TX, 1980).
[31] T. B. Benjamin, J. Fluid Mech. **2**, 554 (1957).
[32] S. J. Weinstein and K. J. Ruschak, Annu. Rev. Fluid Mech. **36**, 29 (2004).
[33] E. Pitts and J. Greiller, J. Fluid Mech. **11**, 33 (1961).
[34] E. I. Parau, J. M. Vanden-Broeck, and M. J. Cooker, J. Fluid Mech. **536**, 99 (2005).
[35] F. W. Pierson and S. Whitaker, Ind. Eng. Chem. Fundam. **16**, 401 (1977).